J. Fluid Mech. (1988), *vol.* 187, *pp.* 353–371
Printed in Great Britain

Three-dimensional Rayleigh-Taylor instability Part 2. Experiment

By J. W. JACOBS† AND I. CATTON
Department of Mechanical, Aerospace and Nuclear Engineering, University of California, Los Angeles, CA 90024, USA

(Received 24 February 1987 and in revised form 29 July 1987)

Three-dimensional Rayleigh–Taylor instability, induced by accelerating a small volume of water down a vertical tube using air pressure, is investigated. Two geometries are studied: a 15.875 cm circular tube and a 12.7 cm square tube. Runs were made with initial disturbances in the form of standing waves forced by shaking the test section in a lateral direction. Accelerations ranging from 5 to 10 times gravitational acceleration and wavenumbers from 1 cm^{-1} to 8 cm^{-1} are studied. The resulting instability was recorded and later analysed using high-speed motion picture photography. Measurements of the growth rate are found to agree well with linear theory. In addition, good qualitative agreement between photographs and three-dimensional surface plots of the weakly nonlinear solution of Part 1 of this series (Jacobs & Catton 1988) is obtained.

1. Introduction

There has been a considerable amount of work devoted to the experimental verification of the theory of Rayleigh–Taylor instability. Attempting to verify Taylor's (1950) linear theory, Lewis (1950) was first to experimentally investigate the instability. In his experiments, liquids were accelerated down a vertical channel, producing an unstable stratified configuration. Using high-speed photography to view the instability, Lewis described three stages of interfacial development. The first stage, which he considered to be valid up until the wave amplitude was approximately $\frac{4}{10}$ the wavelength, was characterized by the growth of the instability being adequately described by linear theory. Lewis described the next stage as a transition region in which the amplitude grew to $\frac{3}{4}$ the wavelength. In the final stage, the instability consisted of round-ended bubbles rising at a constant velocity separated by narrow spikes in approximate free fall.

Allred & Blount (1954) continued the experimental effort begun by Lewis. Using a similar apparatus, they obtained results for situations where the densities of both fluids are approximately equal. For these density ratios, they saw round-ended columns of the heavier fluid penetrating the lighter fluid instead of the sharp spikes usually observed with large density differences. In the later stages of development, they observed a Kelvin–Helmholtz instability in which the vertical sides of the troughs rolled into vortex-like structures. The results of Allred & Blount did not agree well with the theory of Taylor and they attributed this disagreement to the fact that they had to use two liquids for their fluids (instead of a gas and a liquid). In doing so, the diffusion of one medium into the other tended to 'smear' the interface, thus

† Present address: California Institute of Technology, Pasadena, CA 91125.

reducing the growth rate. Duff, Harlow & Hirt (1962) had a similar problem with their experiments using two gases. Emmons, Chang & Watson (1960) performed experiments in which they were able to include the effects of surface tension. Their results agreed well with the theory of Bellman & Pennington (1954), except in the vicinity of the cutoff wavenumber. This disagreement was later explained by the nonlinear theory of Nayfeh (1969). More recent experimental work has been reported by Cole & Tankin (1973), Ratafia (1973) and Popil & Curzon (1980)

All the experiments mentioned above have one thing in common: they were all done in cavities with long narrow geometry, intending to isolate the two-dimensional instability. The work we present here differs from those investigations in that the instability in a fully three-dimensional environment is studied. The experimental apparatus we use is similar in principle to the ones used by Lewis (1950) and Allred & Blount (1954), differing only in that we use tubes of circular and square cross-section. Jacobs *et al.* (1985) looked at Rayleigh–Taylor instability produced in a circular enclosure without forced initial conditions. This work may be considered a continuation of that investigation. Here we shall look at two geometries (square and circular) and, in order to obtain better controlled experiments, initial conditions are forced by gently shaking the test section in a lateral direction.

2. Experimental apparatus and procedure

Rayleigh–Taylor instability was produced in these experiments by accelerating a small volume of water down a vertical tube using air pressure. Figure 1 is a schematic of the experimental apparatus as it appears just prior to the start of a run. It consists of a cylindrical air tank, approximately 90 cm in diameter and 280 cm long, connected to a vertical tube. The connection from the tank to the vertical tube is made through an elbow and bellows expansion joint, shown in the drawing. The upper section of the tube is standard 6 in. schedule 40 aluminium, while the lower half (the test section) is Plexiglas. The test section is divided in two parts with a piece of very thin (0.008 mm) aluminium foil clamped in the joint to isolate the two sections. A Teflon disk and an overlying layer of water rest on top of the foil. The upper surface of the water provides the interface where the instability is produced, while the disk, sized so that it slides freely in the test section, is used to ensure that the bottom surface of the water remains flat as it is accelerated down the tube. Suspended immediately below the upper diaphragm is a cutter made of a smaller steel tube, its bottom edge lined with razor blades. The cutter is temporarily held in place with an electromagnet. The bottom end of the test section is sealed with another heavier piece of aluminium foil. Initially, the sections of tube above and below the liquid layer are pressurized equally; the bottom section is then isolated from the rest of the system by the activation of a solenoid valve. To initiate a run, the current to the electromagnet is disconnected, releasing the cutter which falls under its own weight and breaks the bottom diaphragm. This depressurizes the bottom chamber. The added force caused by the pressure difference is enough to break the thinner diaphragm, forcing the water and disk to accelerate down the tube.

Neglecting friction forces acting between the water and disk against the tube wall, and assuming that the pressure above and below the assembly remains constant, the water will experience a net downward acceleration of magnitude.

$$g = \frac{PA}{M} - g_0, \tag{2.1}$$

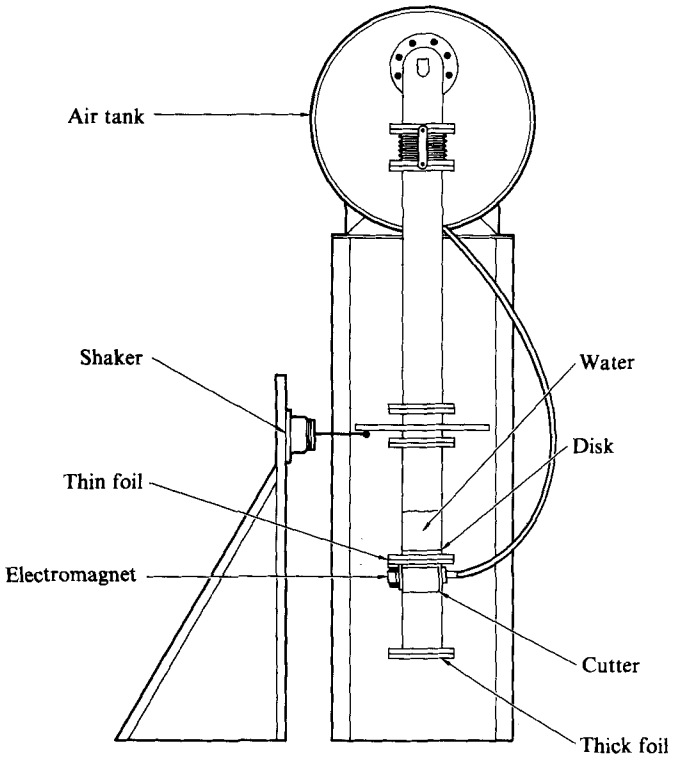

FIGURE 1. Schematic of the experimental apparatus.

where M is the mass of the water and disk, P is the initial tank pressure, A is the cross-sectional area of the tube and g_0 is gravitational acceleration.

Two test sections were used in this study. Shown in figure 1 is the circular test section, made from two pieces of cast acrylic tube with an 15.875 cm inside diameter. A square test section, constructed from four pieces of 1.27 cm thick acrylic sheet, glued to form a tube with a 12.7 cm square cross-section, was also used.

Initial conditions were generated by gently shaking the test section in a lateral direction. An MB Electronics model EA1250 vibration exciter (shown in figure 1 bolted to a stand) was used to shake the test section. The shaker is coupled to the test section with a rod and a ball joint. The driving signal for the exciter was provided by a Hewlett-Packard model 202c low-frequency oscillator. The signal was fed through a MB Electronics 2120MB power amplifier which boosted it enough to drive the exciter.

The instability was visualized using high-speed motion-picture photography, taken from two vantage points. One camera was positioned in front of the apparatus to record the instability from the side, while the other was placed at the top of the vertical pipe looking down through a port in the elbow to provide a top view of the instability. Both were Hycam 16 mm rotating-prism-type cameras, operated at 1000 frames per s. A 50 mm focal-length lens was used with the top camera to provide a close view of the interface. Use was made of a longer 75 mm focal-length lens with the front camera to reduce parallax errors. Lighting was provided by three 650 W quartz floodlights, placed behind a translucent acrylic sheet and positioned to provide an illuminated background for the side camera. Two additional 1000 W

floodlights were positioned in front of the apparatus to provide fill lighting for the side camera. These also served to provide light for the upper camera by illuminating the upper side of the Teflon disk. Black-and-white Kodak 4-X 7277 reversal film was used.

The experimental procedure required a series of events to be triggered in rapid succession during a run. This was accomplished using a cascade of time-delay circuits which, when activated, (1) start the cameras, (2) close the solenoid valve isolating the bottom part of the test section from the tank, (3) cut off the shaker signal, and (4) release the electromagnet, all at the proper time. A more detailed description of the experimental apparatus and procedure can be found in Jacobs (1986).

3. Results and discussion

3.1. *Runs in the circular test section*

A series of runs were made in the circular test section with initial conditions consisting of sloshing-type standing waves (i.e. modes, antisymmetric about a plane passing through the axis of the tube). This motion produced initial free-surface deflections of the form

$$\eta = F(t)\cos\theta J_1(k'r'). \tag{3.1}$$

Wavenumbers k' varying from 1.08 cm^{-1} to 7.81 cm^{-1} were forced. In all of these runs, 3 l of water ($d' = 15$ cm) was accelerated at either $5g$ or $10g$.

In an earlier investigation using this apparatus (Jacobs *et al.* 1985), the acceleration of the slug of water was measured by recording the location of the disk as a function of time off of the film. Linear regression was then used to fit this data to a second-order polynomial; and from this the acceleration was determined. In the runs described here, the side-view camera was moved closer to the test section to provide pictures with greater resolution. In this new position, the disk was no longer within the camera's view. Thus, there was no good reference point with which to track the motion of the liquid slug, making the measurement of acceleration difficult. Measurements were initially made using the interfacial contact line as a reference point; however, they did not provide sufficiently consistent results. In the runs described here, the water was carefully measured, the disk was accurately weighed and the system pressure was accurately monitored prior to a run. The errors made in measuring the mass of the liquid and disk and in the measurement of pressure were less than 1 %. Estimates of the drag of the water and disk against the tube wall were found to be less than 1 % of the pressure force which drives the system. Thus, it is felt that in these experiments, the acceleration is given to reasonable accuracy by (2.1) with the appropriate measurements. This was verified by the earlier set of runs described above, which revealed (2.1) to be in error by no more than $0.2g$.

Table 1 contains data obtained from these runs. In all cases the acceleration was determined as described above. With knowledge of the mode being forced (easily predicted by the forcing frequency) and the tube diameter, the wavenumber can be calculated using

$$k'_n = \frac{j'_{1,n}}{R'}, \tag{3.2}$$

where $j'_{1,n}$ is the nth zero of the Bessel function J_1, and R' is the tube radius. Also given in table 1 are the cutoff parameter $K \equiv k'/k'_c$ and the dimensionless linear growth rate $\sigma_1 \equiv \sigma'_1/(gk')^{\frac{1}{2}} = (1-K^2)^{\frac{1}{2}}$.

Figure 2 gives a sequence of views of the instability in run C3. The photographs show that, initially, the shape of the interface is predominantly that of a single

run	g/g_0	n	k' (cm^{-1})	K	σ_1	σ	ϵ
C1	10.0	10	3.87	0.333	0.943	0.75	0.107
C2	10.0	6	2.28	0.196	0.981	1.13	0.051
C3	10.0	3	1.08	0.093	0.996	0.99	0.119
C4	10.0	20	7.81	0.672	0.741	0.87	0.019
C6	10.0	10	3.87	0.333	0.943	0.92	0.050
G1	5.0	3	1.08	0.131	0.991	1.04	0.100
G2	5.0	6	2.28	0.277	0.961	0.99	0.044
G3	5.0	10	3.87	0.471	0.882	0.89	0.041
G4	5.0	15	5.86	0.713	0.701	0.78	0.021
G5	5.0	20	7.81	0.950	0.312	0.37	0.032

TABLE 1. Runs in the circular test section

Fourier mode. As time progresses, the crests become sharper and more narrow while the troughs become broader and more rounded. Later on, the centre crest takes on a spike-like appearance while the centremost trough forms an almost spherical bubble. Similarly, the outer crest forms a sharp ridge. Figure 3 provides views of another run with a higher wavenumber. Again the shape of the interface initially resembles that of a single Fourier mode with the crests becoming narrower, and the troughs broader as time progresses. In the later stages of development, the centremost crest forms a droplet appearing as though it will eventually separate from the surface. The other crests form a series of thin sheets, reminiscent of the petals of a flower; while the corresponding troughs form annular bubbles which eventually breakup into smaller more spherical bubbles. Similarly, the centremost trough forms a spherical bubble, growing at a greater rate than the others.

Owing to the close proximity of the side camera in these runs, the side view of the instability could be recorded only for as long as shown in figures 2 and 3. The top camera provided views much later in time. These films showed gradual destruction of the spatially periodic structure of the initial disturbance into what appeared to be turbulence. This process is discussed in greater detail in Jacobs *et al.* (1985).

Crest heights were measured in these runs with the aid of a graphics tablet. This tablet is able to determine the location of a stylus when positioned on its surface, and then send these coordinates to a dedicated microcomputer which records them on magnetic tape. The side-view films were projected onto the tablet and the film plane x- and y-coordinates of the wave crests were recorded. To obtain an estimate of the mean surface elevation, the position of the portion of the contact line closest to the camera as well as the portion that was furthest were recorded. The y-coordinates of these points were then averaged to obtain the y-coordinate of the centrepoint of the meniscus plane. The crest amplitude was then determined by subtracting the crest y-coordinate from this centrepoint. The side-view films for these runs were taken at a slight angle of elevation (approximately 10°); so the measurements had to be corrected for this viewing angle. The digitized data was converted into physical units using the tube diameter (digitized at the beginning of each session) as a reference length.

A time sequence of crest heights were obtained for each run. These included the centremost crest and then as many others as were clearly visible. The centremost crest, being the largest and most clearly visible, always provided the best data (even

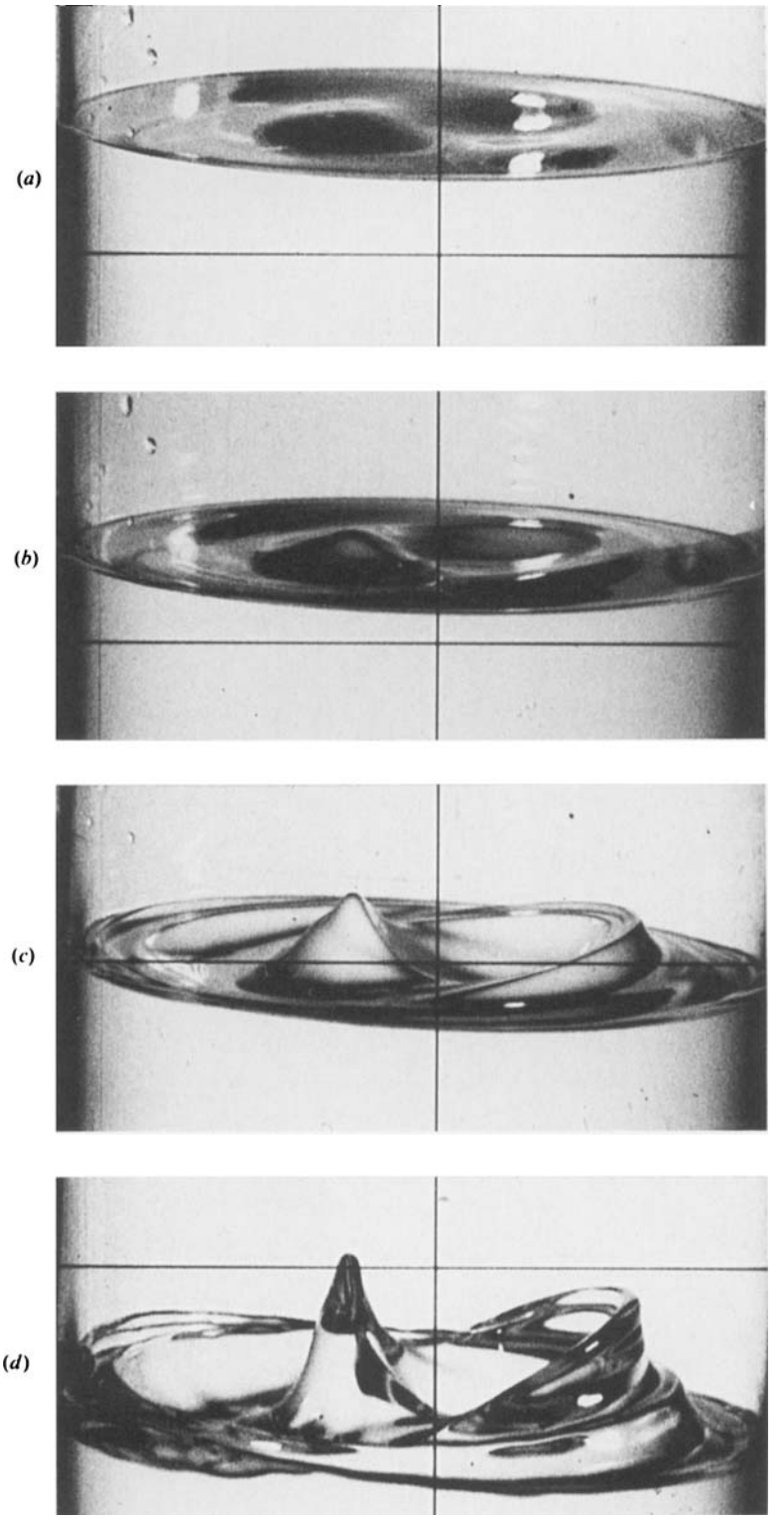

FIGURE 2. A sequence of photographs taken from the film of run C3. (*a*) $t = 5$ ms, with measured centre-crest height $\eta' k' = 0.37$; (*b*) $t = 15$ ms, $\eta' k' = 0.68$; (*c*) $t = 25$ ms, $\eta' k' = 1.77$; (*d*) $t = 35$ ms, $\eta' k' = 3.79$.

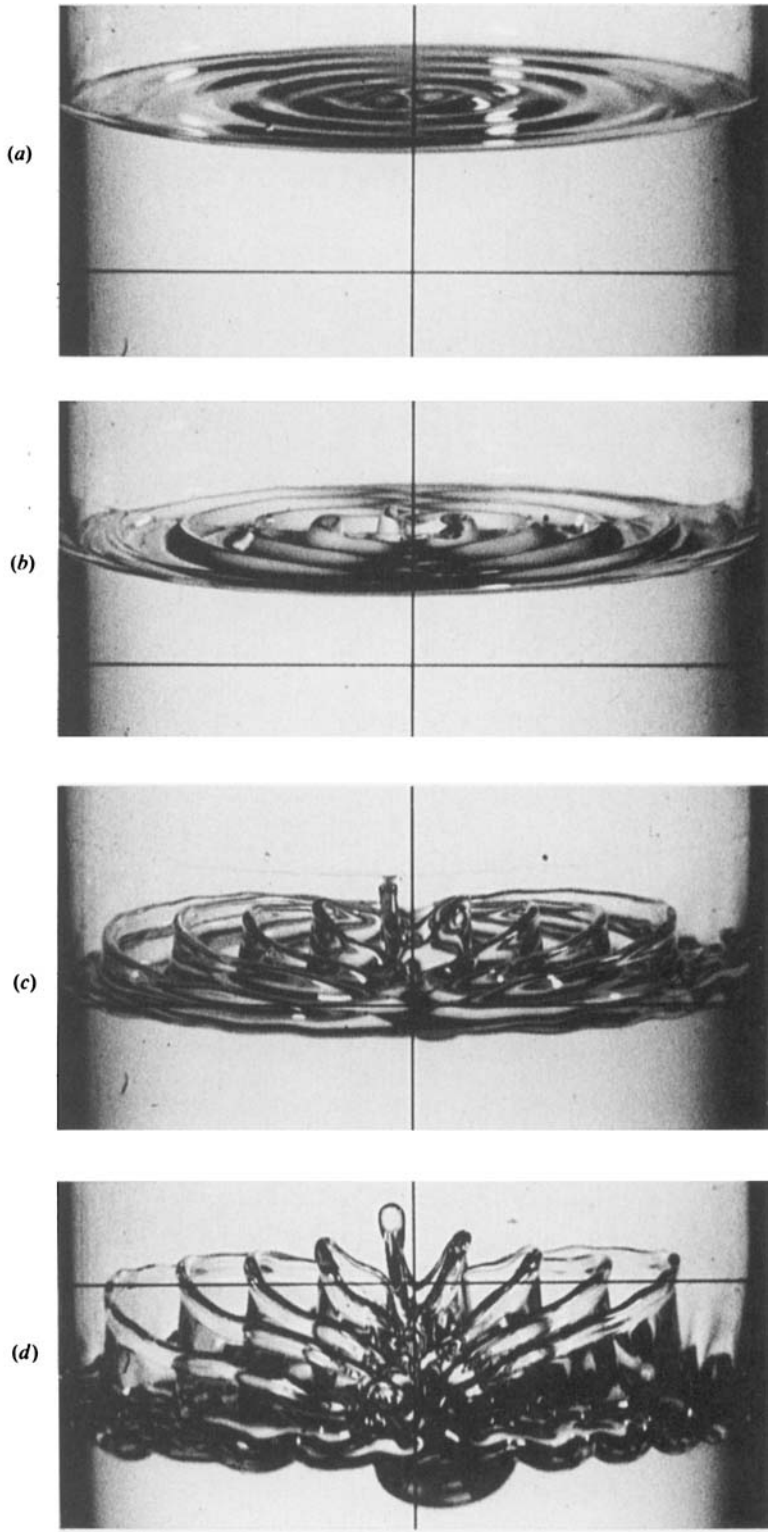

FIGURE 3. A sequence of photographs taken from the film of run C6. (*a*) t = 5 ms, with measured centre-crest height $\eta' k' = 0.66$; (*b*) $t = 15$ ms, $\eta' k' = 3.09$; (*c*) $t = 25$ ms, $\eta' k' = 8.41$; (*d*) $t = 35$ ms, $\eta' k' = 18.6$.

better than a weighted average of all the crests). As a result, only the centre-crest data were used. The initial amplitude η_0' was determined by averaging the measured amplitude over the first few frames at the beginning of each run; then the r.m.s. slope ϵ was calculated using

$$\epsilon = \frac{[1-(R'k')^{-2}]^{\frac{1}{2}} J_1(R'k')}{\sqrt{2}J_1(j_{1,1}')} \eta_0' k'. \tag{3.3}$$

The error induced in the crest height measurements as a result of the accuracy of the graphics tablet is less than 0.05 mm; however, there may be greater error in these measurements caused by the uncertainty of the exact location of a crest tip when viewed on the films. The measurement of elapsed time was accomplished using timing marks placed on the film by the high-speed cameras. The error in time measurements as a result of fluctuations in the film speed is estimated to be less than 0.05 ms. Because of the uncertainty of the exact starting time, there may be an error in the location of the origin by as much as 2 ms.

If the growth of the surface waves were purely exponential (i.e. $\eta \sim e^{\sigma t}$), a plot of $\ln(\eta)$ versus t would yield a straight line with slope equal to the growth rate σ. In reality, the growth (even of the linear instability) is rarely purely exponential. Linear theory predicts the growth to be given by a linear combination of $\sinh(\sigma t)$ and $\cosh(\sigma t)$. The logarithms of these functions approach straight lines as $t \to \infty$; however, they are not linear near $t = 0$. We know from the analysis of Part 1, (Jacobs & Catton 1988) that nonlinear saturation will cause the finite-amplitude instability to grow at a rate less than exponential, and that this effect increases with increasing amplitude. Thus, we expect a plot of $\ln(\eta)$ versus time to diverge from the straight line given by purely exponential growth both near $t = 0$ and as $t \to \infty$. If the initial amplitude is small enough, there will be a section in the centre portion of the plot of $\ln(\eta)$ that is very nearly linear and with slope nearly equalling the growth rate.

Say that a run is initiated with conditions such that the linear growth is given by $\eta \sim \cosh(\sigma t)$. The plot of $\ln(\eta)$ versus time would look like the curve marked $\cosh(x)$ in figure 4. This curve starts at $x = 0$ with zero slope, then approaches a straight line with slope equal to σ as $t \to \infty$. As the amplitude becomes large, nonlinear saturation becomes increasingly more important, causing the amplitude to fall below linear theory as shown in the figure (dashed line), and giving the plot of the nonlinear instability an S-shaped appearance. If the initial amplitude is small enough, the slope of the centre portion of the curve will be a good approximation to the linear growth rate, making the linear growth rate approximately equal to the maximum slope. Now suppose that the instability is started with initial conditions giving the linear growth of $\eta \sim \sinh(\sigma t)$. The plot of $\ln(\eta)$ versus time would now look like the curve marked $\sinh(x)$ in figure 4. Just as before, the linear growth rate of this instability is equal to the slope in the central portion of the curve; however, this time the slope at the point of minimum second derivative will give an accurate measurement of linear growth rate.

Table 1 contains the dimensionless measured growth rate $\sigma \equiv$ measured growth rate$/(gk')^{\frac{1}{2}}$ for the runs in the circular test section, determined using the criteria described above. Linear regression was used to fit line segments to selected portions of data, allowing the slope of these curves to be determined. Only data falling inside a time window of length equal to one growth constant $(1/\sigma_1)$ was used in the regression. The window was allowed to traverse the data giving a sequence of slopes. The largest slope in the sequence was taken as the growth rate. In all cases the time window contained at least five points. Run G5 was unique in that the data for this

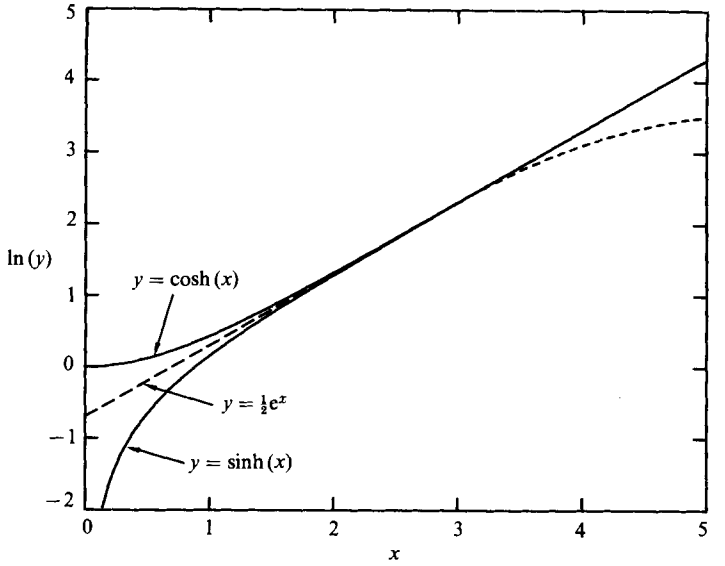

FIGURE 4. A plot of the logarithm of several exponential functions.

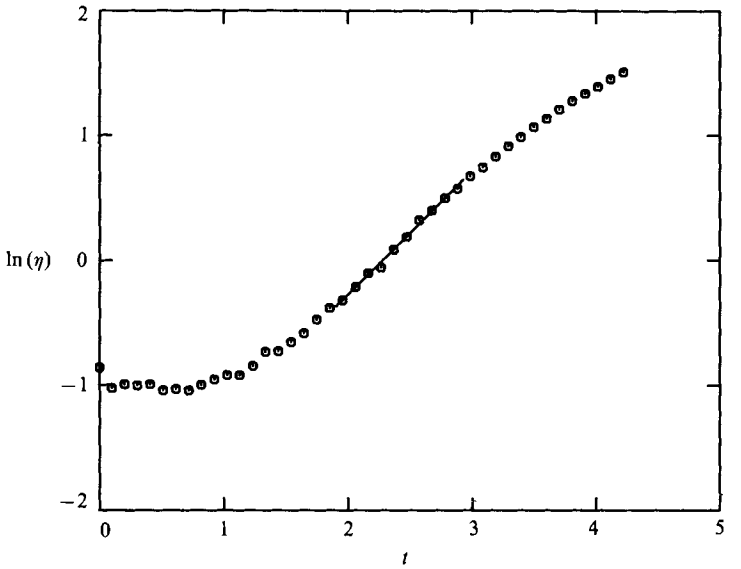

FIGURE 5. The logarithm of the centre-crest height for run C3, along with the line fit to the section providing the maximum slope.

run passes through zero indicating that the solution had a hyperbolic sine component. For this run the slope at the point of minimum second derivative was used to obtain the growth rate. Figure 5 is a log–linear plot of the data of run C3 along with the line fit to the section providing the maximum slope. Figure 6 is a plot of the growth rates given in table 1 along with a line representing linear theory. Although there is a lot of scatter in the data, caused by the inaccuracy of the crest height measurements, the data are distributed evenly over the line, indicating good agreement with linear theory.

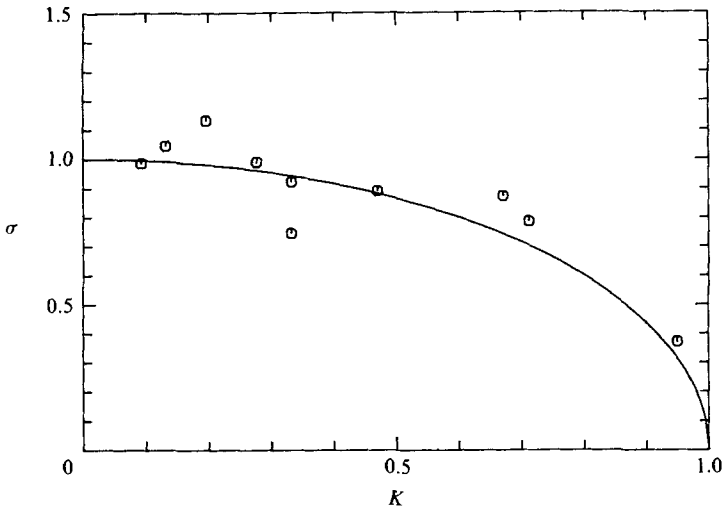

FIGURE 6. Measured growth rate versus K for the runs in the circular test section, along with a line giving the value predicted by linear theory.

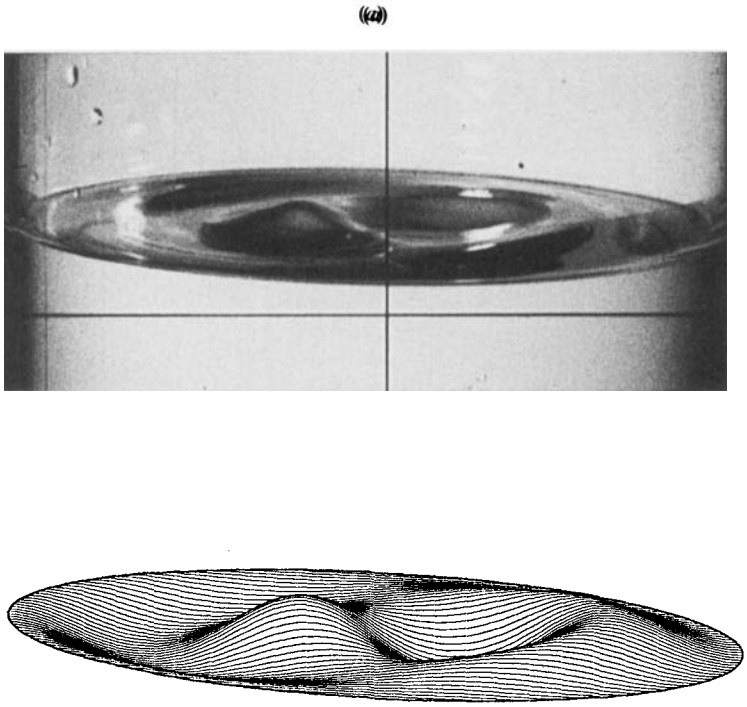

FIGURE 7(*a*). For caption see facing page.

In all cases the crest elevation in the intervals giving the measured growth rates of figure 6 were such that $\eta' k' \approx 1$. Thus, growth rates within 10% of linear theory were obtained for amplitudes up to $\eta' k' \approx 1$. Lewis (1950) found his growth-rate measurements to drop below 50% of the linear theory value when the amplitude reached $\eta' k' \approx 2.5$; and considered the instability to be in good agreement with linear theory for amplitudes below this point. In contrast, a similar analysis of the data

(*b*)

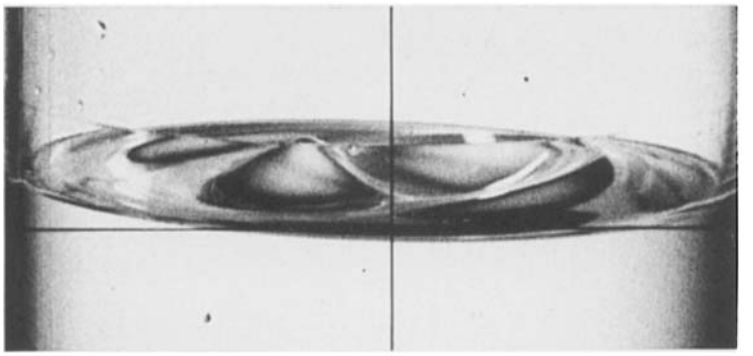

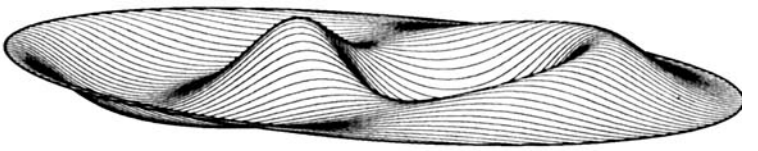

(*c*)

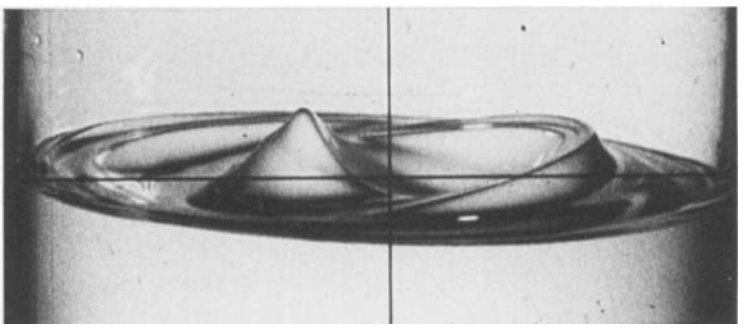

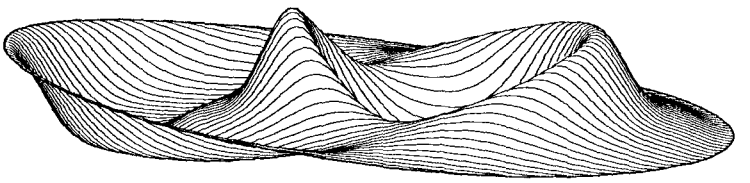

FIGURE 7. A comparison of photographs taken from the film of run C3 and three-dimensional plots of the asymptotic solution with $\epsilon = 0.119$, $K = 0.0929$ and (*a*) $t = 1.545$, (*b*) $t = 2.06$ and (*c*) $t = 2.575$.

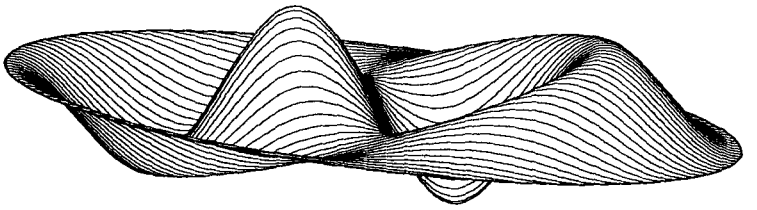

Linear theory

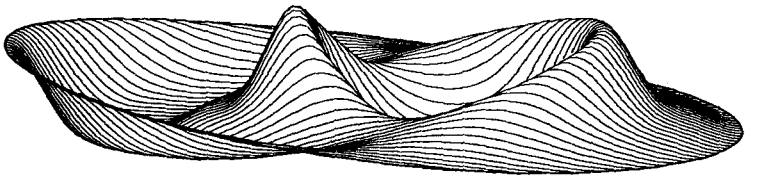

Nonlinear theory

FIGURE 8. A comparison of solutions calculated using linear and weakly nonlinear theory with $\epsilon = 0.119$, $K = 0.0929$ and $t = 2.575$.

presented here shows the measured growth rate to drop below 50% of linear theory when $\eta' k' \approx 5$. It is interesting to note that the weakly nonlinear solution developed in Part 1 (Jacobs & Catton 1988) was found to break down at $\eta' k' \approx 0.5$. Thus, linear theory has proven itself to be valid for significantly larger amplitudes than the weakly nonlinear theory.

Figure 7(*a–c*) compares photographs taken from run C3 to surface plots of the asymptotic solution of Part 1 with parameter values chosen to match the experiment ($\epsilon = 0.119$, $K = 0.0929$ and $t = 1.545$, 2.06 and 2.575). The agreement between experiment and theory as observed in this figure is very good. Figure 8 is a comparison of the nonlinear solution of figure 7(*c*) with linear theory. In this comparison the effects of the nonlinear analysis can easily be seen. Although the amplitudes of the two solutions are very close, the differences in shape are considerable. The nonlinear solution is much better at capturing the actual shape of the instability shown in the photographs. In particular, the nonlinear solution is necessary to reproduce the sharpness of the crest tips.

3.2. *Runs in the square test section*

Runs were made in the square test section with initial conditions forced by shaking the test section in the same way as for the circular geometry. Runs were first made forcing the test section in a direction perpendicular to a side of the square tube. This type of forcing produced standing waves which were predominantly two-dimensional; however, when runs were made using these two-dimensional waves as initial conditions, the instability that resulted was not two-dimensional but was instead entirely three-dimensional. All of the runs made under these conditions developed instabilities having roughly square planform with wavenumbers equalling that of the forced two-dimensional initial disturbance. Thus, a two-dimensional instability could not be produced in these experiments.

With this in mind, runs were then made with initial conditions forced by shaking

run	g/g_0	n	k' (cm^{-1})	K	σ_1	σ	ϵ
D1	10.0	27	6.68	0.575	0.819	0.87	—
D2	10.0	21	5.19	0.446	0.895	0.89	—
D3	10.0	15	3.71	0.319	0.948	0.80	—
D4	10.0	9	2.23	0.192	0.981	1.05	0.096
D6	10.0	5	1.24	0.107	0.994	0.97	0.061
D7	10.0	33	8.16	0.702	0.712	0.72	—
E2	5.0	27	6.68	0.813	0.583	0.67	—
E3	5.0	21	5.19	0.631	0.776	0.72	—
E4	5.0	15	3.71	0.451	0.892	0.86	0.141
E5	5.0	9	2.23	0.271	0.963	0.97	0.200
E7	5.0	5	1.24	0.151	0.989	1.02	0.069

TABLE 2. Runs in the square test section

the test section in a direction running diagonally across the square tube. This excitation produced square-type standing waves with initial surface deflections of the form

$$\eta = F(t)[\cos(k'x') + \cos(k'y')]. \tag{3.4}$$

Wavenumbers k' ranging from 1.24 cm^{-1} to 8.16 cm^{-1} were forced. In each of these runs 2 l of water ($d' = 12.4$ cm) was accelerated at either $5g$ or $10g$. Table 2 gives a list of these runs. The values given for acceleration and wavenumber in table were determined in the same manner as for the circular geometry except that in this case the wavenumber is given by

$$k' = \frac{n\pi}{X'}, \tag{3.5}$$

where X' is the width of the square test section.

Figure 9 is a sequence of views taken from the film of run E7; and figure 10 shows views taken from a run with higher wavenumber. In these photographs, the instability initially appears in the form of a single doubly periodic Fourier mode. As time increases the surface shape changes, with the crests becoming narrower and the troughs wider. Like pictures taken of the two-dimensional instability, the surface shape in these photographs takes on a cusped appearance. In the later stages of development the instability consists of an array of spikes interlaced by a grid of more or less spherical bubbles, arranged such that each bubble is surrounded by four spikes. The spikes are connected by a network of thin sheets of liquid which form boundaries around the bubbles. Very late in the run the spike tips form an array of pendant-like drops which appear as though they will eventually separate from the rest of the liquid.

Wave amplitudes were measured in a slightly different way in these runs. In this geometry, minima as well as maxima in surface elevation along a line perpendicular to the line of sight (x' = constant) could easily be observed in the films. Given that the surface shape is described by (3.4), the maxima correspond to crests and the minima correspond to points where $\eta = 0$ (nodes). The difference in elevation between the crests and nodes can then be measured to obtain the amplitude. Another important difference between the circular and square geometries is that in the square geometry the wave amplitude is more or less uniform throughout the tube. This means that elevations of several crests and nodes can be measured in each frame and then averaged to obtain a more reliable value. In the runs described here, several

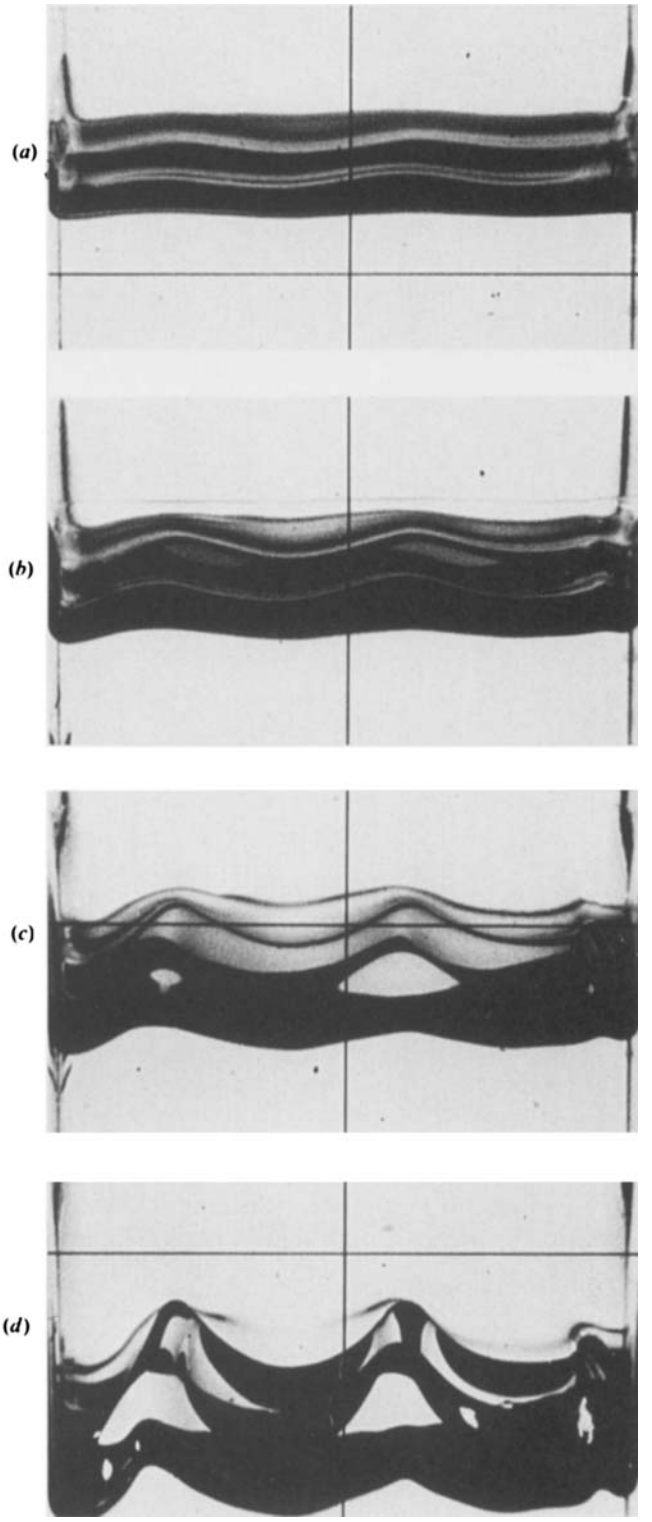

FIGURE 9. A sequence of photographs taken from the film of run E7. (a) $t = 20$ ms, with measured crest height $\eta' k' = 0.30$; (b) $t = 30$ ms, $\eta' k' = 0.56$; (c) $t = 40$ ms, $\eta' k' = 1.06$; (d) $t = 50$ ms, $\eta' k' = 1.71$.

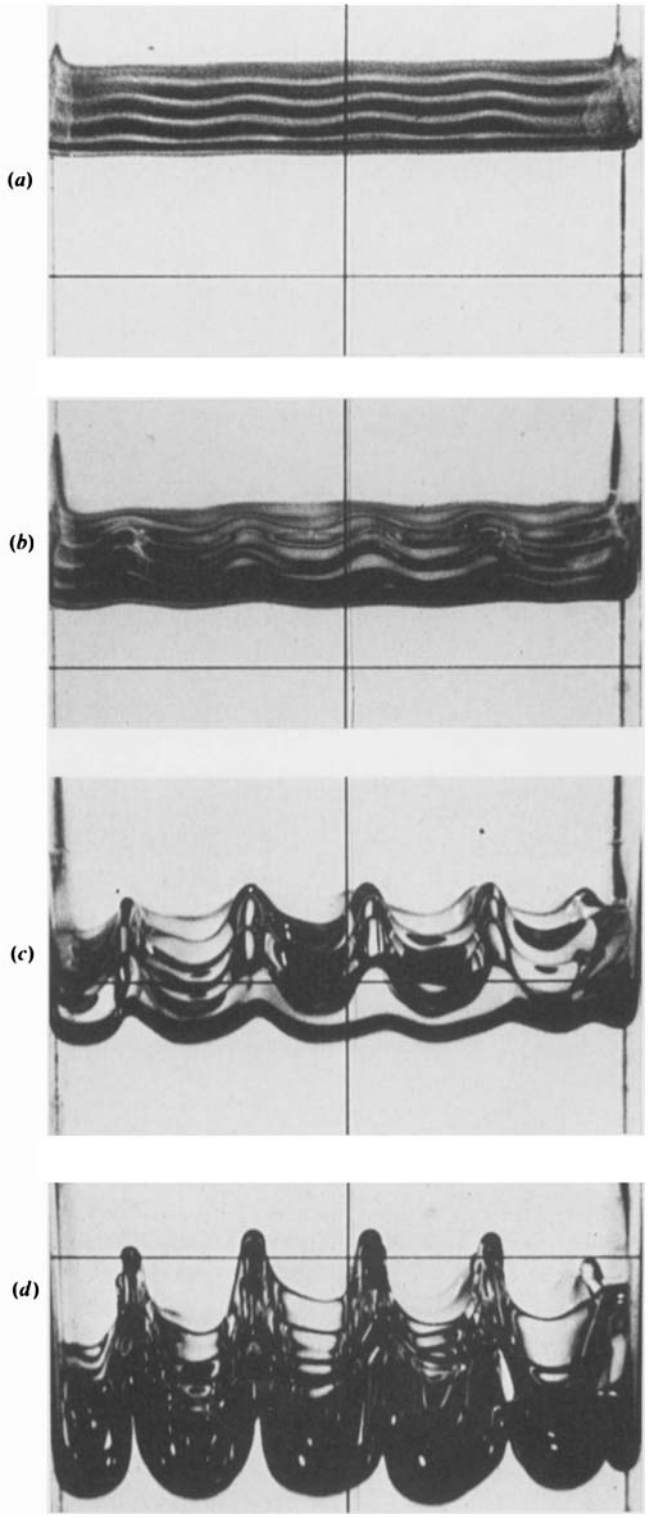

FIGURE 10. A sequence of photographs taken from the film of run D4. (*a*) $t = 5$ ms, with measured crest height $\eta' k' = 0.28$; (*b*) $t = 15$ ms, $\eta' k' = 0.88$; (*c*) $t = 25$ ms, $\eta' k' = 2.77$; (*d*) $t = 35$ ms, $\eta' k' = 4.63$.

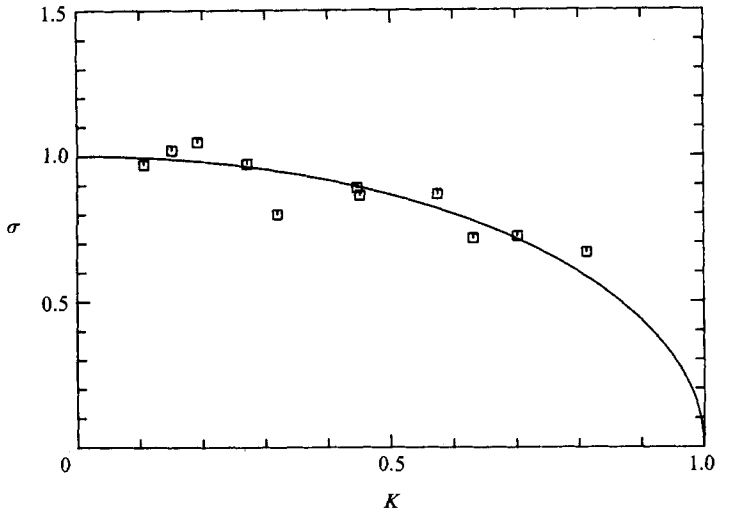

FIGURE 11. Measured growth rate versus K for the runs in the square test section along with a line giving the value predicted by linear theory.

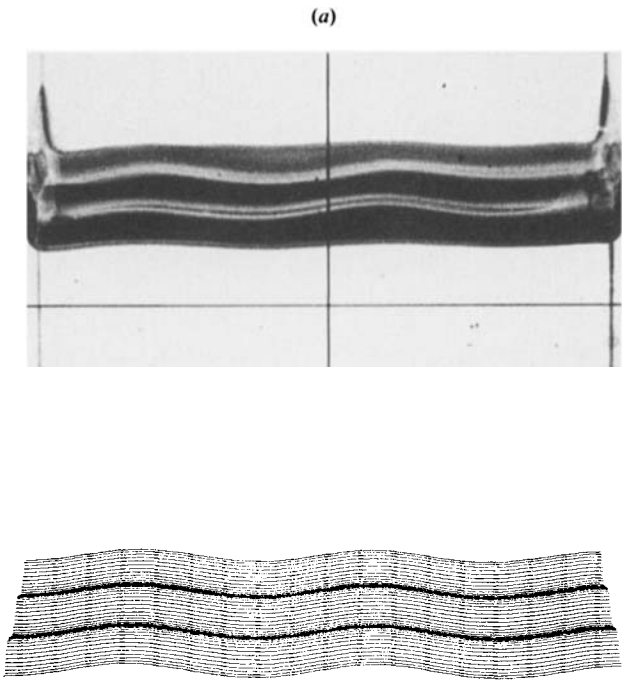

waves (four to eight) were chosen to be measured. In each frame the elevations of the chosen crests along with an equal number of neighbouring nodes were determined. As before, measurements were obtained with the aid of a graphics tablet. The heights of the crests were then averaged, and the same was done for the nodes. The average node elevation was then subtracted from the average crest height to obtain the amplitude. The measurements were then corrected for the viewing angle and converted into physical units in the same way as was done for the circular geometry.

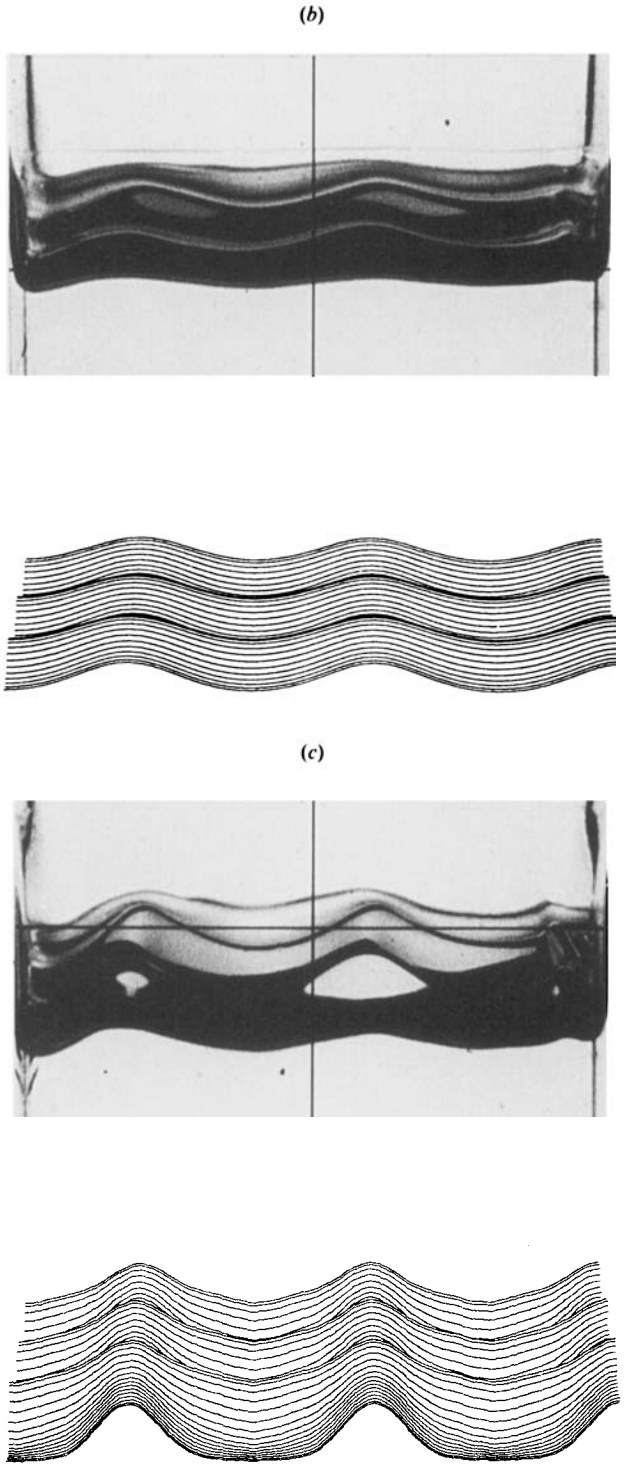

FIGURE 12. A comparison of photographs taken from the film of run E7 and three-dimensional plots of the asymptotic solution with $\epsilon = 0.069$, $K = 0.1508$ and (*a*) $t = 1.56$, (*b*) $t = 2.34$ and (*c*) $t = 3.12$.

Initial amplitude was determined in the same way in these runs as for the circular geometry, except in this geometry ϵ is given by

$$\epsilon = \tfrac{1}{2}\eta_0' k'. \tag{3.6}$$

In some cases the initial amplitude was too small to be measured; thus ϵ is missing for some of the runs in table 2.

Growth rates were determined in the same manner as for the circular geometry. These values are listed in table 2 and are plotted in figure 11 along with a line representing linear theory. There is noticeably less scatter in figure 11 than the corresponding plot for the circular geometry (figure 6), owing to the effect of averaging the measurements. As in the circular geometry, there is good agreement between the measured growth rates and linear theory.

The average crest heights in the intervals giving the measured growth rates of figure 11 were also calculated in these runs. This data again revealed that measured growth rates within 10% of linear theory were obtained with amplitudes up to $\eta' k' \approx 1$. Figure 12(*a–c*) is a comparison of photographs taken from the film of run E7 with surface plots of the asymptotic solution using $\epsilon = 0.069$, $K = 0.1508$ and $t = 1.56$, 2.34 and 3.12. Again the agreement between experiment and theory is quite good.

4. Conclusions

Three-dimensional Rayleigh–Taylor instability was produced in square and circular geometries with initial disturbances consisting of sloshing-type standing waves, forced by gently shaking the test section in a lateral direction. Photographs of the instability revealed networks of spikes and sheets of liquid separating nearly spherical bubbles or two-dimensional troughs. Crest heights were measured, and from these measurements growth rates were determined. This data revealed that good agreement with linear theory can be obtained for amplitudes up to $\eta' k' \approx 1$. This is rather surprising considering that the validity of linear theory is based on the assumption that $\eta' k' \ll 1$. In Part 1 (Jacobs & Catton 1988) we found that the weakly nonlinear solution breaks down at $\eta' k' \approx 0.5$; thus, linear theory appears to be valid for amplitudes significantly greater than the weakly nonlinear theory. Good agreement was found between experiment and the nonlinear analysis when comparing photographs with three-dimensional surface plots of the asymptotic solution; thus, nonlinear theory is much better at predicting the shape of the instability.

Several conclusions can be made. Linear theory is effective in predicting the growth rate of the instability well into the nonlinear regime, and is valid much later in time than the weakly nonlinear analysis. Even though the weakly nonlinear analysis is valid only for a short time, it is necessary and effective in predicting certain surface shape characteristics of the nonlinear instability, such as the sharpening of crests and the broadening of troughs. It may be noted that the weakly nonlinear analysis is able to show the effect of geometry on the growth of the instability; however, this effect is too small to be verified by measurements in these experiments.

This work was supported by the National Science Foundation under grant MEA 81-05542.

REFERENCES

ALLRED, J. C. & BLOUNT, G. H. 1954 Experimental studies of Taylor instability. *Los Alamos Scientific Laboratory rep.* LA-1600.

BELLMAN, R.& PENNINGTON, R. H. 1954 Effects of surface tension and viscosity on Taylor instability. *Q. Appl. Maths* **12**, 151–162.

COLE, R. L. & TANKIN, R. S. 1973 Experimental study of Taylor instability. *Phys. Fluids* **16**, 1810–1815.

DUFF, R. E., HARLOW, F. H. & HIRT, C. W. 1962 Effects of diffusion on interface instability between gases. *Phys. Fluids* **5**, 417–425.

EMMONS, H. W., CHANG, C. T. & WATSON, B. C. 1960 Taylor instability of finite surface waves. *J. Fluid Mech.* **7**, 177–193.

JACOBS, J. W. 1986 Three-dimensional Rayleigh–Taylor instability: experiment and theory. Ph.D. dissertation, University of California, Los Angeles.

JACOBS, J. W., BUNSTER, A., CATTON, I. & PLESSET, M. S. 1985 Experimental Rayleigh–Taylor instability in a circular tube. *Trans. ASME* I: *J. Fluids Engng* **107**, 460–466.

JACOBS, J. W. & CATTON, I. 1988 Three-dimensional Rayleigh–Taylor instability. Part 1. Weakly nonlinear theory. *J. Fluid Mech.* **187**, 329–352.

LEWIS, D. J. 1950 The instability of liquid surfaces when accelerated in a direction perpendicular to their planes. II. *Proc. R. Soc. Lond.* A **202**, 81–96.

NAYFEH, A. H. 1969 On the non-linear Lamb–Taylor instability. *J. Fluid Mech.* **38**, 619–631.

POPIL, R. & CURZON, F. L. 1980 Climbing water films in experiments on Rayleigh–Taylor instabilities. *Phys. Fluids* **23**, 1718–1719.

RATAFIA, M. 1973 Experimental investigation of Rayleigh–Taylor instability. *Phys. Fluids* **16**, 1207–1220.

TAYLOR, G. I. 1950 The instability of liquid surfaces when accelerated in a direction perpendicular to their planes. I. *Proc. R. Soc. Lond.* A **201**, 192–196.